Lab on a Chip

Cite this: *Lab Chip*, 2012, **12**, 3952–3960

www.rsc.org/loc

PAPER

Double spiral microchannel for label-free tumor cell separation and enrichment†‡

Jiashu Sun,§*[a] Mengmeng Li,§[ac] Chao Liu,[b] Yi Zhang,[a] Dingbin Liu,[a] Wenwen Liu,[a] Guoqing Hu*[b] and Xingyu Jiang*[a]

Received 29th April 2012, Accepted 2nd July 2012
DOI: 10.1039/c2lc40679a

This work reports on a passive double spiral microfluidic device allowing rapid and label-free tumor cell separation and enrichment from diluted peripheral whole blood, by exploiting the size-dependent hydrodynamic forces. A numerical model is developed to simulate the Dean flow inside the curved geometry and to track the particle/cell trajectories, which is validated against the experimental observations and serves as a theoretical foundation for optimizing the operating conditions. Results from separating tumor cells (MCF-7 and Hela) spiked into whole blood indicate that 92.28% of blood cells and 96.77% of tumor cells are collected at the inner and the middle outlet, respectively, with 88.5% tumor recovery rate at a throughput of 3.33×10^7 cells min^{-1}. We expect that this label-free microfluidic platform, driven by purely hydrodynamic forces, would have an impact on fundamental and clinical studies of circulating tumor cells.

Introduction

Circulating tumor cells (CTCs), shed from either primary or metastatic cancers, have been identified in the peripheral blood of patients, and are often associated with cancer metastasis and tumor recurrence.[1,2] The majority of deaths from cancer in human patients are caused by metastasis, suggesting an emerging need to precisely isolate and detect CTCs from whole blood.[3–5] Current clinical approaches to isolating CTCs from a blood sample, such as flow cytometry,[6,7] density gradient centrifugation[8,9] and immunocapture using magnetic-bead-based systems,[10,11] are expensive and labor-intensive. These approaches are further complicated by sample pretreatment and lack of specificity and efficiency, because of the extremely low number of CTCs (as little as one cell per 10^9 hematologic cells).[12,13] A method allowing for rapid, easy and sensitive CTC separation and enrichment could therefore have important applications in tumor research and clinical diagnostics.

Recently, much attention has been directed toward microfluidic technologies that can help improve conventional CTC separation techniques with increased detection sensitivity, high separation efficiency, and a significant enrichment factor.[14–24] By fabricating massively antibody-functionalized microposts in a microfluidic chamber, several research groups have successfully demonstrated the high-efficiency and high-purity capture of high-level antigen-expressing CTCs from peripheral blood samples.[17–19] One major challenge of the microfluidic immunocapture lies in the fact that the presence of specific cell-surface markers such as EpCAM or HER-2 on tumors may vary significantly even for the same tumor type, resulting in variable purity of the captured cells, as well as the irreproducible retrieval of isolated CTCs.[14,25]

Another commonly used biological parameter to separate CTCs from blood samples is the cell size. The size of epithelial tumor cells ranges from 15 to 25 μm in diameter, larger than the surrounding blood cells (erythrocytes are 8 μm biconcave disks and peripheral blood lymphocytes are 7–10 μm in diameter).[26–28] Therefore, microfabricated filters with a cutoff pore size of 8 μm have been adopted for CTC enrichment with high capture efficiency and viability.[20,28–30] One limitation of the microfiltration systems is the low processing rate, because the fast flow of a high concentration of blood cells may cause clogging of the devices.[26] To overcome this clogging problem, recent attention has focused on the clever manipulation of the well-controlled laminar flow inside microfluidic channels, which can create size-dependent cell trajectories to separate large CTCs from small blood cells. The particular geometries of microfluidic systems will induce additional hydrodynamic forces, which could be adopted for size-based cell sorting.[31–34] For example, using inertial lift and Dean drag forces in asymmetric serpentine curved channels, the randomly distributed particles of different sizes can be focused into several streams that are size-dependent,

[a]*CAS Key Lab for Biological Effects of Nanomaterials and Nanosafety, National Center for NanoScience and Technology, Beijing, 100190, China. E-mail: sunjs@nanoctr.cn; xingyujiang@nanoctr.cn*
[b]*LNM, Institute of Mechanics, Chinese Academy of Sciences, 100190, China. E-mail: guoqing.hu@imech.ac.cn*
[c]*College of Physics Science, Qingdao University, Qingdao, 266071, China*
† Electronic supplementary information (ESI) available. See DOI: 10.1039/c2lc40679a. Published as part of a themed issue dedicated to Emerging Investigators.
‡ Published as part of a themed issue dedicated to Emerging Investigators.
§ These authors contributed equally to this work.

leading to equilibrium separation at a high flow rate.[35] The particular geometries also include microscale spiral or double spiral, which can completely separate the particle or cell mixture by size based on the differential migration.[36–38] More recently, rectangular microchannels, patterned with a contraction–expansion array, are developed for efficient separation and enrichment of CTCs from peripheral blood in a single step.[39,40]

Inspired by the single spiral cell sorter, here we use a double spiral microfluidic platform with one inlet and three outlets, which allows for passive, label-free tumor cell separation and enrichment. The spiral channel induces a Dean drag force acting on cells to compete with the inertial lift, resulting in large tumor cells being focused and deflected into the middle outlet, while small hematologic cells are removed from the inner outlet. As a demonstration of this technique, we first separated the binary mixture of 5- and 15 μm-diameter polystyrene particles at four different flow rates with an optimal separation efficiency of 99.66% for 5 μm particles and 92.75% for 15 μm particles. We also continuously isolated and enriched the rare tumor cells (MCF-7 and Hela cells) from diluted whole blood using the same geometry. At a spike ratio of 100 tumor cells per million hematologic cells, 92.28% of blood cells and 96.77% of tumor cells were collected at the inner and middle outlet, respectively, at a throughput of 3.33×10^7 cells min^{-1}. We believe this simple double spiral design has the potential to contribute to clinical diagnosis and study of CTCs.

Theory and mechanism

The principle of hydrodynamic separation in curved microfluidic channels is to induce a Dean drag force acting on particles to compete with the inertial lift, resulting in different equilibrium positions for particles of different sizes. Neutrally buoyant particles suspended in curvilinear channels experience the inertial lift force, composed of the shear-gradient-induced lift and the wall effect. The shear gradient lift is caused by the parabolic velocity profile and its associated gradient in shear rate, and is directed from the center of the curvilinear microchannel to the channel wall; the wall effect is induced by the asymmetric wake of the particle near the wall and tends to push the particle away from the wall.[31] The competition of the two effects results in particles focusing on specific equilibrium positions. The inertial lift force responsible for particles migrating away from the channel center and walls, can be theoretically predicted as:[41,42]

$$F_L = f_L(\mathrm{Re}, x_L) \cdot \rho U^2 a^4 / {D_h}^2 \quad (1)$$

where the lift coefficient f_L is a function of the channel Reynolds number Re ($\mathrm{Re} = \rho U D_h/\mu$) and the particle position x_L within the cross-section of the channel (the distance to the channel center). U is the maximum velocity within the microchannel, ρ and μ are the density and the dynamic viscosity of the fluid, respectively, D_h is the hydrodynamic diameter of the microchannel (four times the channel cross section divided by the perimeter), and a is the particle diameter. According to eqn (1), the particle size has a dramatic influence on this lateral lift force, which is the underlying mechanism for creating distinct equilibrium positions for particles of different sizes.

At a relatively high Reynolds number, a secondary cross-section flow (Dean flow) will develop in curved microchannels, due to the non-uniform inertia of the fluid in the inner and outer segments. The secondary flow consists of two counter-rotating Dean vortices forming in the top and bottom halves of the channel, and exerts additional transverse drag forces on particles that alter the position of flowing particles. Here, a dimensionless Dean number (De) is defined to characterize the flow in a curved channel:

$$\mathrm{De} = \mathrm{Re}\sqrt{D_h/R} \quad (2)$$

where R is the curvature radius. The magnitude of the Stokes drag force on suspended particles due to this secondary flow is given by:[43]

$$F_D \sim \rho U^2 a D_h^2 / R \quad (3)$$

Like inertial lift force, Dean drag is also directed perpendicularly to the primary flow, but leads to the mixing of particles. The interaction between inertial lift and Dean drag will determine the final equilibrium positions of suspended particles (Fig. 1). When the magnitude of the Dean drag is comparable to that of the inertial lift forces, particles are focused on a single equilibrium position or array contributing to the secondary flow.

In this work, we design a double spiral microchannel with 6-spiral loops for each direction (Fig. 1(a)). In contrast to most previous work on the hydrodynamic separation of biological objects in curved geometry,[36,37,43,44] our double spiral microchannel (300 μm wide and 50 μm high) has a very low aspect ratio ($H/W = 0.167$) and an alternation of flow direction through the S-turn, both of which are critical parameters determining the

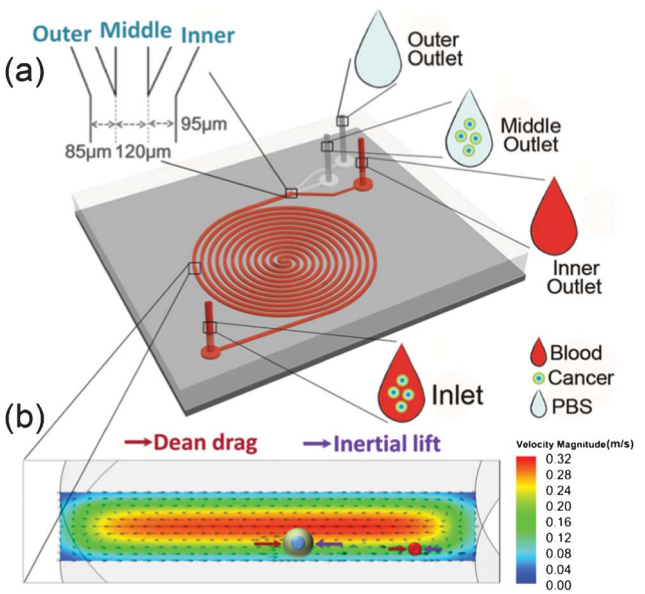

Fig. 1 (a) Schematics of the microfluidic cell sorter containing 6-loop double spiral microchannels with one inlet and three outlets for particle/cell separation. (b) Illustration of the two counter-rotating Dean vortices forming in the top and bottom halves of the channel. The black arrows represent the velocity field in the cross section. The competition between inertial lift and Dean drag leads to distinct equilibrium positions for the large tumor cells and the small blood cells.

separation performance. In the low aspect ratio microchannel, the much greater shear rate across the channel height pushes the particles to the z-direction equilibrium positions very quickly. During the motion through the loops of the channel, particles mainly migrate along the channel width to the final equilibrium positions. We only display the lift forces in the x and y directions in Fig. 1(b), since the positions of particles along the channel height do not affect the separation performance in the end.

Materials and methods

Device design and fabrication

The device design consists of a 6-loop double spiral microchannel with one inlet and three outlets. The planar microchannel first rotates in the counterclockwise direction for 6 loops, changes the direction through an S-shaped junction, then rotates in the clockwise direction to form the double spiral. The double spiral microchannel has a low aspect ratio ($H/W = 0.167$) with dimensions of 300 μm in width and 50 μm in height, and the spacing between two adjacent loops is 450 μm. The radius of the outermost curvature is 9 mm. The widths of the inner outlet (the outlet close to the double spiral channel), the middle outlet and the outer outlet are 85 μm, 120 μm and 95 μm, respectively, as depicted in Fig. 1(a).

The microfluidic device was fabricated using standard soft-lithography with an SU8-2050 master mold on a silicon substrate.[45–47] Degassed PDMS (mixed in a 10 : 1 ratio of PDMS base with curing agent, Sylgard 184, Dow Corning Inc.) was cast over the mold and baked at 80 °C for 3 h in an oven. The PDMS with embedded channels was subsequently diced by razor blade and removed from the master mold. One inlet and three outlets were punched through the PDMS using a needle with a flattened tip. The PDMS slab was then bonded with a glass substrate (25 mm × 75 mm) post oxygen plasma treatment. A plastic tube was inserted through the inlet port and secured by the liquid PDMS on top of the device. The assembled device was finally placed into an oven at 70 °C for 30 min to cure the liquid PDMS and seal the intersection seam between the PDMS and the tube.

Numerical simulations

For a complex microfluidic system, numerical simulation has become an effective tool to quantitatively examine how different factors affect the particle dynamics. In this work, a three-dimensional double spiral geometry was modeled using the commercially available computerized fluid dynamics (CFD) software Fluent (version 6.4, Fluent Inc.). The Navier–Stokes equations for flow fields without particles were first solved using a second order upwind scheme, along with the SIMPEC algorithm for pressure–velocity coupling. Nonslip boundary conditions were implemented on the channel walls. A pressure boundary condition was applied at the channel inlet to match the flow rates used in experiments, while an atmospheric pressure was fixed at the triple outlets. After the steady flow field was obtained numerically, the particle trajectories were then tracked by integrating the force balance based on Newton's second law of motion:

$$\frac{\mathrm{d}\vec{v}_\mathrm{P}}{\mathrm{d}t} = \frac{18\mu}{\rho_\mathrm{P} a^2}\frac{C_\mathrm{D}\mathrm{Re}_\mathrm{s}}{24}\left(\vec{v}-\vec{v}_\mathrm{P}\right) + \frac{\vec{g}(\rho_\mathrm{P}-\rho)}{\rho_\mathrm{P}} + \frac{1}{2}\frac{\rho}{\rho_\mathrm{P}}\frac{\mathrm{d}\left(\vec{v}-\vec{v}_\mathrm{P}\right)}{\mathrm{d}t} + \frac{F_\mathrm{L}}{\frac{1}{6}\pi a^3 \rho_\mathrm{P}} \quad (4)$$

where t is the time, $\vec{v}_\mathrm{P}$ is the velocity vector of the particles, $\vec{v}$ is the flow velocity, $\vec{g}$ is the gravitational acceleration, and ρ_P is the density of the particles. Eqn (4) was derived by integrating the force balance based on Newton's second law of motion. On the right hand side of the equation, the first term is the drag force per unit particle mass, the second term caused by gravity can be ignored since the particle/cell density is almost the same as the density of the suspending medium, the third term represents the virtual mass force to accelerate the fluid surrounding the particle, and the last term is the inertial lift force. The drag coefficient C_D can be calculated by $C_\mathrm{D} = a1 + \frac{a2}{\mathrm{Re}_\mathrm{s}} + \frac{a3}{\mathrm{Re}_\mathrm{s}^2}$, where the values of $a1$, $a2$, $a3$ are taken from Morsi and Alexander[42] according to the relative Reynolds number $\mathrm{Re}_\mathrm{s} = \frac{\rho a|\vec{v}-\vec{v}_\mathrm{P}|}{\mu}$. The last term, acceleration caused by the inertial lift F_L, was added using a user defined function (UDF) in Fluent.

Sample preparation

5 μm-diameter and 15 μm-diameter polystyrene microspheres fluorescently labeled with green and red, respectively, were purchased from Phosphorex, Inc. The suspension of 5 μm particles or 15 μm particles was diluted in deionized water containing 0.1% w/v Tween 20 (AMRESCO Inc.). Two types of particles were mixed in a 1 : 1 ratio (v/v) to achieve a mixture concentration of 1×10^6 particles mL^{-1} (the concentration ratio of the two types of particles is 1 : 1).

Two human carcinoma cell lines, MCF-7 (average diameter around 18 μm) and HeLa (average diameter around 13 μm) were chosen as models for CTC separation and enrichment.[15,39] MCF-7 and HeLa cells were grown to confluence in high-glucose Dulbecco's modified Eagle's medium (DMEM) supplemented with 10% fetal bovine serum (FBS) and 1% penicillin–streptomycin in a 5% CO_2, 37 °C incubator (Thermo Scientific). Human whole blood drawn from healthy volunteers was collected into 3 mL EDTA vacuum tubes, and diluted by ratios of 1 : 20, 1 : 50, 1 : 100, and 1 : 200 with 1× PBS, corresponding to hematocrit values of 2%, 1.25%, 0.4% and 0.2%, respectively. Hela cells, MCF-7 cells, and diluted whole blood were stained with C3099 (0.5%, green), C34551 (0.5%, orange), and C3099 (0.5%, green) for about 1 h, respectively. After staining, cells were centrifuged at 900 rpm for 3 min, and resuspended in PBS (1×). The concentration of MCF-7 or Hela cells was counted with a hemocytometer. To model the low events of CTCs in blood, we spiked a small amount of fluorescently labeled MCF-7 and Hela cells into unstained 50× diluted blood. Different tumor (MCF-7 and Hela cells) to blood cell ratios of 1×10^{-4} (0.01%) and 1×10^{-6} were prepared, and the final concentrations of tumor cells in diluted blood samples were 10,000 cells mL^{-1} and 100 cells mL^{-1}, respectively. The total cell concentration of the mixture was 1×10^8 cells mL^{-1}.

Experiment set-up

In the experiment of separating the particle mixture, the double spiral microchannel was first primed with deionized water. A binary mixture of polystyrene particles was introduced to the double spiral microchannel using a syringe pump (Longer Precision Pump Co., Ltd.) connected to the microchannel through the inlet plastic tube. The flow rate inside the microchannels was precisely controlled by adjusting the parameters of the pump. Similarly, in the experiment of separating tumor and blood cells, the double spiral channel was first filled with PBS, followed by loading the mixture solution of MCF-7, Hela and blood cells *via* the pump. The assembled device was mounted onto the stage of a Leica DMI 6000 microscope (Leica Microsystems). Fluorescent streak images at different excitation and emission wavelengths were obtained using a CCD camera with an exposure time of 5 s. The composite fluorescence images were created using Adobe Photoshop CS4 (Adobe Systems Inc.). The image analysis software Image-Pro Plus (Media Cybernetics) was used to measure the fluorescence intensity of captured images. In addition, three-dimensional fluorescence images illustrating the distribution of 5 μm (red) and 15 μm (green) particles were visualized and analyzed using a Zeiss LSM 710 confocal microscope system (Carl Zeiss).

Results and discussion

Separation of binary polystyrene particles

Using commercial CFD software Fluent, we began with the 3D numerical simulation of flow fields and particle motion in the 6-loop double spiral microchannel with one inlet and three outlets, as shown in Fig. 1. The simulation prediction of the velocity field at the S-shaped junction indicated a reversal in the direction of the Dean vortex for consecutive anticlockwise and clockwise spirals (Fig. S1†). We simulated the motions of a binary mixture of 5- and 15 μm-diameter particles under four flow rates: 10 mL h^{-1}, 15 mL h^{-1}, 20 mL h^{-1}, and 25 mL h^{-1}. In all simulations, the particles were randomly injected into the spiral channel at different x, y and z positions (Fig. S2†). Fig. 2 displays the trajectories of 5 μm (red) and 15 μm (blue) particles near the trifurcated outlet. Under a low flow rate of 10 mL h^{-1}, the larger 15 μm particles were focused into a thin stream while the smaller 5 μm particles were still spread over quite a large part of the cross section. When the flow rate increased to 15 mL h^{-1} and 20 mL h^{-1}, the 5 μm particles became focused into one position. However, the 15 μm particles were distributed not only on the previous equilibrium position but also on a second inner position (Fig. 2(b,c)). For a further increased flow rate of 25 mL h^{-1}, this inner position became the only equilibrium position for the 15 μm particles (Fig. 2(d)). In the spiral microchannel, the Dean drag force acting on the particles is proportional to the square of the flow velocity. At a flow rate of 25 mL h^{-1}, 15 μm-diameter particles will experience a stronger Dean drag directed toward the inner wall, resulting in migration of the equilibrium position toward the inner wall. It is worth noting that the final focusing positions of particles in our double spiral channel are different from those observed by other researchers.[36,37] We believe that such a dramatic change in equilibrium positions arises from the low channel aspect ratio and the double spiral configuration, which play a critical role in determining the inertial migration of particles in confined microchannels. One possible explanation is: since the inertial lift is proportional to the fourth power of the diameter of the particles, while the Dean drag is proportional to the diameter, the competition between the two forces determines the discrete equilibrium positions of the different sized particles. In the double spiral channel, small particles are more easily influenced by Dean flow, and tend to migrate towards the inner wall. In comparison, the inertial force on large particles dominates over the Dean drag along the double spiral. In the first spiral, the large particles focus closer to the inner wall, as observed by other researchers (Fig. S2†).[36,38] Since the inner wall becomes the outer wall in the second spiral after the S-turn, the position of the large particles is now located near the centerline, while the position of the small particles switches to the inner wall (previously the outer wall in the first spiral). The large particle stream remains predominantly constant with decreasing De number, due to the large lift force.

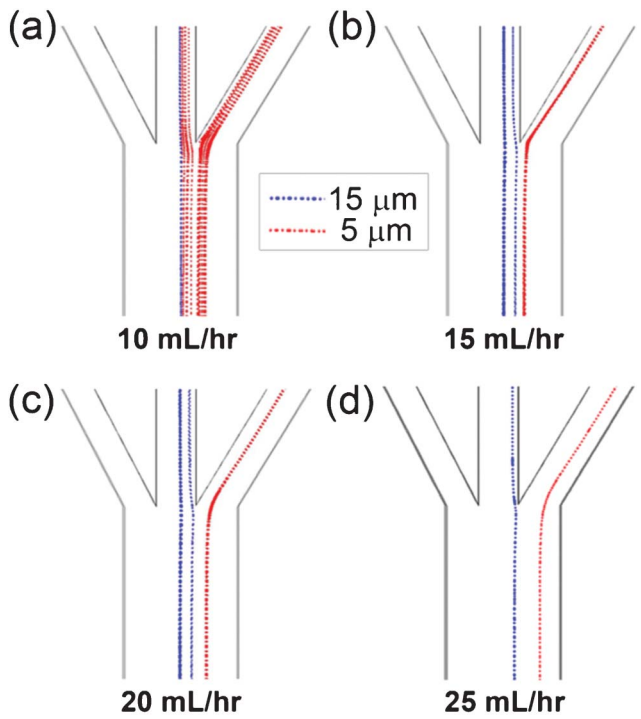

Fig. 2 Simulation prediction of the trajectories of two types of particles near the trifurcated outlet of the double spiral microchannel. (a) Flow rate 10 mL h^{-1}; (b) flow rate 15 mL h^{-1}; (c) flow rate 20 mL h^{-1}; (d) flow rate 25 mL h^{-1}. The red and blue dashed lines denote 5 μm particles and 15 μm particles, respectively.

Based on the numerical simulations, we first characterized the performance of the device by separating the binary mixture of 5- and 15 μm-diameter fluorescently labeled particles. Using flow rates of 10, 15, 20 and 25 mL h^{-1}, controlled by the syringe pump, the particle mixture was introduced into the double spiral channel through the inlet. Higher flow rates were not investigated because the required high pressure drop may result in leakage of the microfluidic device. Given the channel dimensions and the flow rates, we can derive the corresponding Reynolds numbers and Dean numbers from eqn (1) and (2) (Table 1). The composite fluorescence images were created to show the trajectories of the 15 μm (red stream) and 5 μm particles (green

Table 1 The statistical results of separation efficiency for a binary mixture of 5- and 15 μm-diameter polystyrene particles

Flow rate (mL h^{-1})	Reynolds number	Dean number	Inner outlet 5 μm (%)	Middle outlet 15μm (%)
10	24	2	99.67 ± 0.76	41.73 ± 2.85
15	36	3	98.72 ± 0.79	88.70 ± 0.67
20	48	4	99.66 ± 0.49	92.75 ± 2.54
25	60	5	95.09 ± 1.64	89.84 ± 1.57

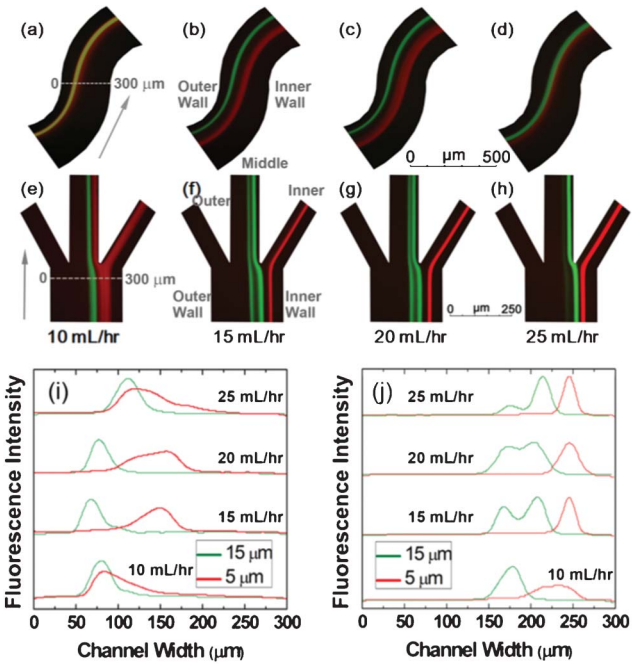

Fig. 3 Composite fluorescence images showing the trajectories of the 5 μm (red stream) and 15 μm (green stream) particles at (a–d) the center, and (e–h) the trifurcated outlet of the double spiral channel at varying flow rates ranging from 10 to 25 mL h^{-1}. (i) Line scans across the 300 μm wide channel of each composite image taken at the center to illustrate the distribution and position of 5 μm and 15 μm particles. (j) Line scans across the channel width of each composite image taken at the outlet. The red and green lines denote the 5 μm particles and the 15 μm particles, respectively.

stream) at the center (Fig. 3 (a–d)) and the trifurcated outlet (Fig. 3(e–h)) of the double spiral channel at various flow rates or Reynolds numbers. The line scans were taken across the 300 μm wide channel of each composite image, and analyzed using Image-Pro Plus software to illustrate the distribution and position of the 15 μm (red) and 5 μm particles (green) at the center (Fig. 3 (i)) and at the trifurcated outlet (Fig. 3(j)).

As seen in Fig. 3(i), a tendency toward particle separation was observed at the flow rates of 15 and 20 mL h^{-1} at the center of the double spiral channel. After particles passed the S-turn and reached the trifurcated outlet (Fig. 3(j)), the stream of 5 μm particles was focused to a thinner band (~40 μm wide) at a flow rate above 10 mL h^{-1}, while the 15 μm particles were distributed over two equilibrium positions (two green peaks) at the same flow rate. Finally, most 15 μm particles flowed out through the middle outlet and most 5 μm particles went out through the inner outlet. To provide the position of large and small particles along the spiral channel, we recorded the fluorescent trajectories of 5- (red stream) and 15 μm-diameter (green stream) polystyrene particles in each loop of the double spiral at a flow rate of 20 mL h^{-1} (Fig. S3†). The experimental and statistical results (Fig. S3 and S4†) show that for the originally randomly distributed 5- (red stream) and 15 μm-diameter (green stream) polystyrene particles (Loop 1), a tendency toward particle separation occurred at the innermost loop (Loop 6) after particles traversed 6 loops in the counterclockwise direction. After particles passed the S-shaped junction (Loop 6′) and migrated out in the clockwise direction through the outermost loop (Loop 1′), a more clear particle separation was observed, as well as a narrower focused stream of 5 μm particles, revealing a better focusing and separation performance of the double spiral microchannel. Based on the fluorescent streaks along the double spiral microchannel, we estimated that the entry distance for particles becoming focused was around 65 mm (Loop 2) for large particles, and 106 mm (Loop 3) for small particles. We also noted that once the 15 μm particles became focused, their position was around the centerline of the channel (Fig. S3†).

These experimental observations were in good agreement with our numerical simulation results (Fig. 2). The confocal fluorescence microscopy images displaying the 3-D distribution of 5 μm (red) and 15 μm (green) particles at the center (Fig. S5(a)†) and the outlet (Fig. S5(b)†) also confirmed this particle separation at a flow rate of 20 mL h^{-1} (for details see ESI†). To quantify the separation performance, we captured a series of microscopic images at the inner and the middle outlet and counted more than 200 particles for each flow rate. The separation efficiency is defined as the percentage of 15 μm particles (or 5 μm particles) in the middle (or inner) outlet. At the optimal flow rate of 20 mL h^{-1} (Re = 48), a high separation efficiency of 99.66 ± 0.49% for 5 μm particles and 92.75 ± 2.54% for 15 μm particles was achieved (Table 1).

Separation of tumor cells from human blood

Similarly, we performed numerical simulations to assess the focusing and separation efficiency of the designed device for three different kinds of cells. The MCF-7, Hela, and blood cells were represented by the 18 μm, 13 μm, and 6 μm diameter particles in the simulations, respectively. Fig. 4 depicts the trajectories of the MCF-7 (red), Hela (green), and blood (blue) cells near the trifurcated outlet of the double spiral microchannel, at four different flow rates: 10, 15, 20, and 25 mL h^{-1}. It clearly shows that within quite a wide range of flow rates, the two larger cells (MCF-7 and Hela) can be successfully focused and separated from the blood cells using the present microchannel configuration. On the other hand, these numerical predictions were validated by the following experiments on cell focusing and separation, too.

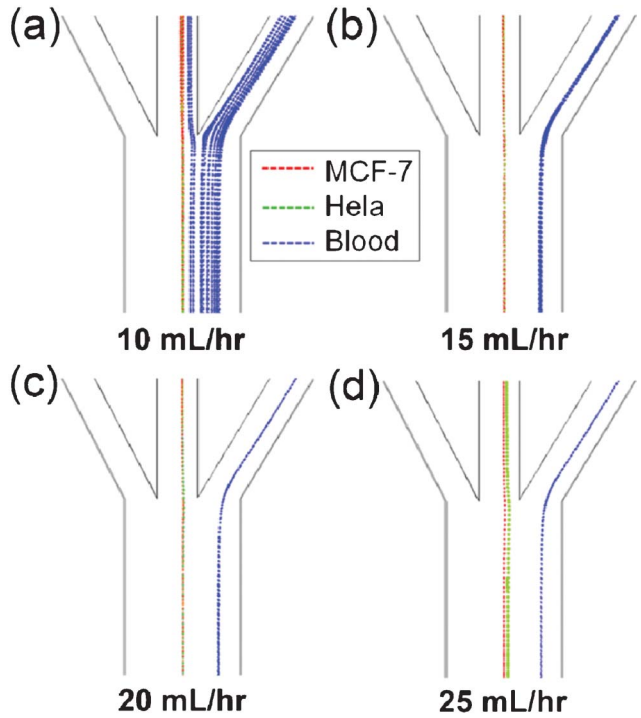

Fig. 4 Simulation prediction of trajectories of MCF-7, Hela and blood cells near the trifurcated outlet of the double spiral microchannel. (a) Flow rate 10 mL h^{-1}; (b) flow rate 15 mL h^{-1}; (c) flow rate 20 mL h^{-1}; (d) flow rate 25 mL h^{-1}. The red, green and blue dashed lines denote the MCF-7, Hela and blood cells, respectively.

To investigate the effect of hematocrit on blood cell focusing in the low-aspect-ratio microchannel, we first conducted the experiments with diluted whole blood samples (0.2% to 2% hematocrit) at a flow rate of 20 mL h^{-1} (Fig. 5). The results revealed that the width of the focused blood stream became wider in an approximately linear trend with increasing hematocrit levels, leading to the blood cells contaminating the middle outlet. This phenomenon can be explained as follows: with the increased blood concentration, more blood cells attempted to occupy the same equilibrium positions spontaneously, resulting in enhanced cell–cell interaction and the consequently focusing dispersion.[39,48,49] Thus we chose to use 50× diluted whole blood (0.8% hematocrit) for implementing both the throughput and the focusing performance.

To track the trajectories of three types of cells, we captured and superimposed the fluorescence images of MCF-7 (red stream), Hela (green stream) and blood cells (blue stream) at the center (Fig. 6 (a–d)) and the trifurcated outlet (Fig. 6 (f–i)) at flow rates ranging from 10 to 25 mL h^{-1}. The line scans across the 300 μm channel width at the center (Fig. 6 (e)) suggested a significant overlap among three cell streams, especially at the low flow rate of 10 mL h^{-1}, implying an unsatisfactory separation at the center. However, as cells continued to migrate outward to the trifurcated outlet, tumor and blood cells were separated at flow rates above 15 mL h^{-1} (Fig. 6(f–i)). The distinct equilibrium positions for tumor cells (in the position between 100 and 200 μm) and blood cells (between 225 to 300 μm) led to a size-based cell separation, as the large tumor cells (MCF-7 and Hela cells) flowed out through the middle outlet and the small blood cells went out from the inner outlet. These results agreed well with the simulation predictions, in that at flow rates above 15 mL h^{-1} a separation of tumor and blood cells was achieved (Fig. 4).

We also characterized the position and distribution of the blood, Hela and MCF-7 cells in each loop of the double spiral at a flow rate of 20 mL h^{-1} (Fig. 7 and S6†). For separation of tumor and blood cells with variations in cell sizes (Fig. 7 and S6†), the first spiral cannot order the small blood cells into a narrow stream, and a large degree of overlap still exists between the tumor (red and green) and blood streams (blue) (Loop 1–6 in Fig. 7 and Fig. S6†). As the tumor and blood cells passed the S-shaped junction and traversed along the clockwise direction, the blood cells gradually focused into an attenuated stream, and a separation between tumor and blood cells was finally achieved in Loop 1′. In this manner, the double spiral microchannel presents a much better separation efficiency of blood and tumor cells than the single one. In the current double spiral design, we cannot realize the separation of MCF-7 and Hela cells collected at the middle outlet owing to their small size difference (Fig. 6 and 7). Nevertheless, by optimizing the outlet configuration of the double spiral channel, we might be able to isolate MCF-7 from Hela cells in a future study.

To model the presence of CTCs in human peripheral blood, we spiked a small amount of MCF-7 and Hela cells into 50× diluted whole blood to prepare the cell mixture. The concentration of the

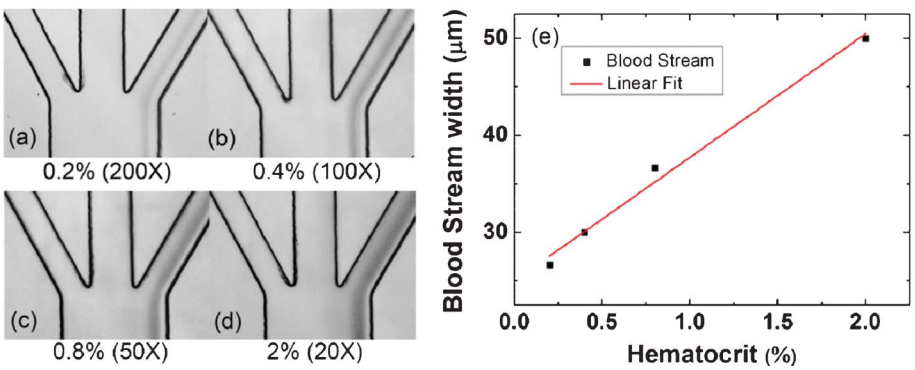

Fig. 5 Bright-field microscopic images illustrating the effect of hematocrit on blood cell focusing at a flow rate of 20 mL h^{-1}. (a) 0.2% hematocrit at 200× dilution; (b) 0.4% hematocrit at 100× dilution; (c) 0.8% hematocrit at 50× dilution; (d) 2% hematocrit at 20× dilution. (e) The linear fit of blood stream width *versus* the hematocrit.

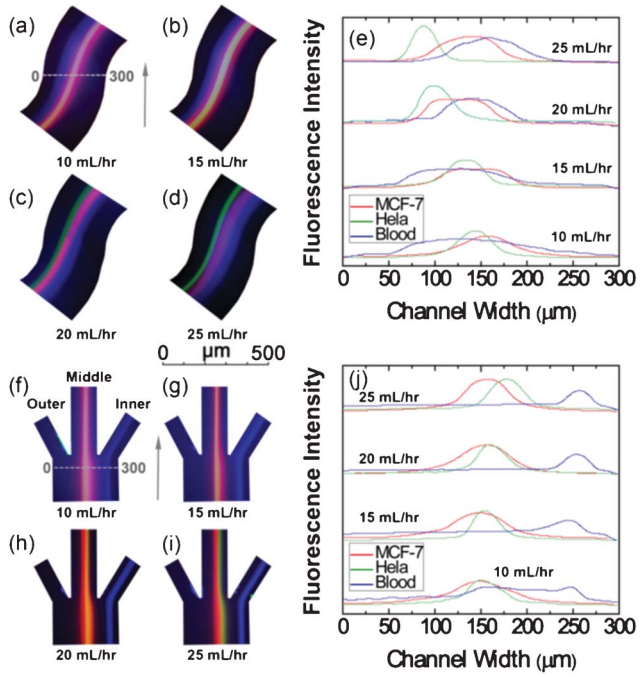

Fig. 6 Composite fluorescence images at (a–d) the center, and (f–i) the trifurcated outlet of the double spiral channel showing the trajectories of MCF-7 (red stream), Hela (green stream) and human blood (pseudo-colored blue stream) at four different flow rates. (e) Line scans across the 300 μm wide channel of each composite image taken at the center to illustrate the distribution and position of MCF-7, Hela, and human blood cells. (j) Line scans across the channel width of each composite image taken at the outlet. The red, green and blue lines denote MCF-7, Hela and blood cells.

cell mixture was 1×10^8 cells mL^{-1}, and the initial concentration ratio of tumor cells (MCF-7 and Hela cells) to blood cells was 0.01% (Fig. 8 (a)). By counting MCF-7 (stained red), Hela (stained green) and blood cells (unstained) in composite images ($N = 10$) taken at random locations of the three outlets at two different flow rates of 10 and 20 mL h^{-1} (Fig. 8(b–d)), we could calculate the enrichment factor of the tumor cells by dividing the ratio of tumor cells to blood cells by the initial tumor-to-blood-cell ratio of 0.01%. Fig. 8e shows that at a flow rate of 10 mL h^{-1} (Re = 24), the enrichment factor of tumor cells at the middle outlet was 6.609 $\pm$ 0.762, due to the inefficient separation. In comparison, at a flow rate of 20 mL h^{-1} (Re = 48), 96.77% of tumor cells and 92.28% of blood cells were collected at the middle and inner outlets, respectively, giving rise to a high tumor enrichment factor of 18.380 $\pm$ 2.642 at the middle outlet with a throughput of 3.33 $\times$ 10^7 cells min^{-1} (Fig. 8(e)). The experiments of tumor cell separation and enrichment were also conducted at an extremely low tumor-to-blood ratio of 1×10^{-6} to mimic the low events of CTCs. The enrichment factors of tumor cells in the middle outlet at flow rates of 10 and 20 mL h^{-1} were 7.173 $\pm$ 1.596 and 19.322 $\pm$ 4.199, respectively, similar to the results obtained at the tumor-to-blood cell ratio of 0.01% (Fig. 8(e)). Moreover, we counted the numbers of MCF-7 and Hela cells before and after separation by analyzing the composite images, and obtained an 88.5% tumor recovery rate, implying a minor loss of tumor cells during the separation. To evaluate the performance of the double spiral channel, we carefully compared our results with the 5-loop single spiral cell sorter.[36] The single spiral microchannel enabled the continuous separation of neuroblastoma (~15 μm in diameter) and glioma (~8 μm in diameter) cells with a separation efficiency of 80% and throughput of 1×10^6 cells min^{-1}. In comparison, our double spiral cell sorter achieved 96.77% separation efficiency for tumor cells (~15 μm in diameter) and 92.28% for blood cells.

Though the high flow rate (20 mL h^{-1}) or Reynolds number (Re = 48) may cause the deformation of tumor cells because of the shear stress acting on them,[50] Fig. 8(c) suggests that both the MCF-7 (red) and Hela cells (green) in the middle outlet kept their intact spherical shape without noticeable cell damage. Recent studies validated that the induced shear stress acting on tumor cells slightly changed their global gene expression profiles, as well as their cell viability at high Reynolds number.[49] Furthermore, we discuss two issues limiting the enrichment factor of tumor cells. One is that the large tumor cells disturb the surrounding flow field and attract the neighboring blood cells by affecting their flow trajectories.[39] The other is that the highly concentrated blood cells (1×10^8 cells mL^{-1}) change the ideal flow pattern in their vicinity and perturb the focusing of the blood to a certain extent.[48] It was also found that deformable tumor cells migrated rapidly toward the channel center line with

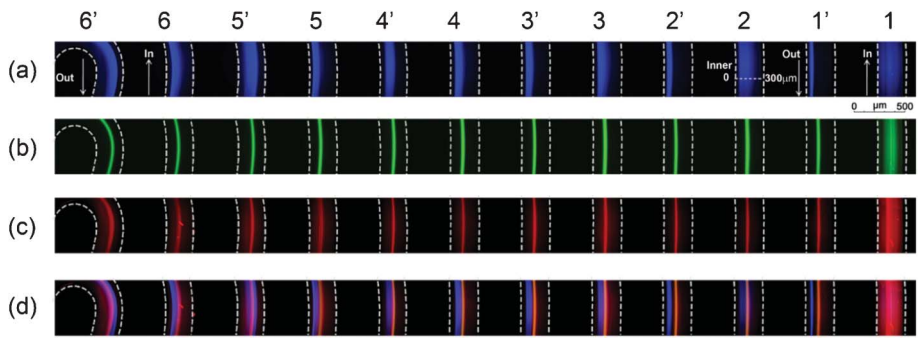

Fig. 7 Fluorescent trajectories of (a) diluted whole blood (blue stream), (b) Hela cells (green stream), and (c) MCF-7 cells (red stream) in each loop along the 6-loop double spiral channel at a flow rate of 20 mL h^{-1}. The cells first migrate toward the center of the double spiral in the counterclockwise direction from Loop 1 to 6, pass the S-shaped junction and migrate out in the clockwise direction from Loop 6′ to 1′. 1 represents the outermost loop in the counterclockwise direction, through which the original randomly distributed cells are introduced into the double spiral channel. 1′ represents the outermost loop in the clockwise direction from which the focused cells flow out. (d) Composite fluorescence image showing the position and distribution of diluted whole blood, Hela and MCF-7 cells.

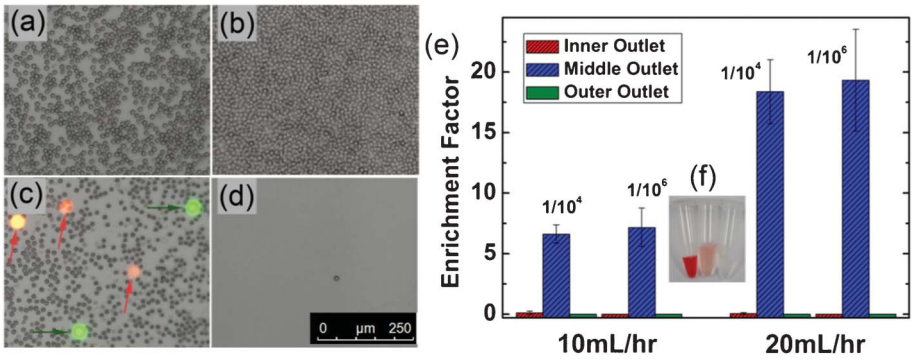

Fig. 8 Composite images of (a) cell mixture before separation, (b) cells collected at the inner outlet, (c) the middle outlet, and (d) the outer outlet at the original tumor-to-blood cell ratio of $1 : 10^4$ (0.01%). MCF-7 and Hela cells are stained with red and green, and indicated by small arrows, while blood cells are unstained. (e) The statistical results of the tumor cell enrichment factors with original tumor-to-blood cell ratios of $1 : 10^4$ (0.01%) and $1 : 10^6$, at two different flow rates of 10 and 20 mL h^{-1}. (f) The bulk samples collected from the inner, middle and outer outlet (left to right) at a flow rate of 20 mL h^{-1} for 100 s.

respect to their rigid polystyrene spherical counterparts.[49] Nevertheless, the separation efficiency would benefit from the deformability of tumor cells, as the hardened small blood cells tended to traverse to the inner channel wall.[51] In our double spiral design, the tumor enrichment factor was around 19, higher than the other passive, label-free microfluidic CTC enrichment techniques.[15,49] More importantly, our passive cell separation technique allows easy retrieval of target cells that remain viable and intact, which could be used for further cell culture, gene analysis, and cancer prognosis. To enhance the separation efficiency and tumor enrichment factor, design of a multiplex cascade of separation circuits or integration of a chip-based downstream filtration system to collect the separated tumor cells should be attempted in a future study.

Conclusions

In this work, we present a passive double spiral microfluidic device, which can separate and enrich tumor cells (MCF-7 and Hela cells) from diluted whole blood continuously with a throughput of 3.33×10^7 cells min^{-1}, an enrichment factor of 19, and a recovery rate of 88.5%. Compared to current technologies for CTC enrichment, such as immuno-binding and microfluidic filtration, our passive double spiral microchannel has certain distinct advantages, including being label-free and clogging-free. Meanwhile, our planar platform can eliminate the need for integration of complex external force fields, making the device easy to fabricate and operate. Compared to the single spiral microchannel, the double spiral device provides better focusing behavior of small blood cells and improved separation efficiency, as well as higher cell throughput. We expect that in future this simple double spiral design can be customized for low-cost and high-efficiency CTC detection, and thus be applied in cancer diagnosis and prognosis.

Acknowledgements

J. S. and X. J. acknowledge financial support from MOST (2011CB933201, 2009CB930001), NSFC (51105086, 21025520, 90813032), and CAS (KJCX2-YW-M15). G. H. acknowledges financial support from MOST (2011CB707604), NSFC (50890182), and CAS (KJCX2-YW-H18). Y. Z. thanks helpful discussions with Dr Wei Wang from Peking University on device fabrication.

References

1 I. Crnic and G. Christofori, *Int. J. Dev. Biol.*, 2004, **48**, 573–581.
2 K. Pantel, R. H. Brakenhoff and B. Brandt, *Nat. Rev. Cancer*, 2008, **8**, 329–340.
3 D. F. Hayes, M. C. Miller, M. Cristofanilli, M. J. Ellis, A. Stopek, W. J. Allard, J. Matera, G. V. Doyle, L. W. W. M. Terstappen and G. T. Budd, *Breast Cancer Res Tr*, 2004, **88**, S225–S225.
4 E. Racila, D. Euhus, A. J. Weiss, C. Rao, J. McConnell, L. W. M. M. Terstappen and J. W. Uhr, *Proc. Natl. Acad. Sci. U. S. A.*, 1998, **95**, 4589–4594.
5 V. Zieglschmid, C. Hollmann and O. Bocher, *Crit. Rev. Clin. Lab. Sci.*, 2005, **42**, 155–196.
6 J. G. Moreno, S. M. O'Hara, S. Gross, G. Doyle, H. Fritsche, L. G. Gomella and L. W. Terstappen, *Urology*, 2001, **58**, 386–392.
7 R. T. Krivacic, A. Ladanyi, D. N. Curry, H. B. Hsieh, P. Kuhn, D. E. Bergsrud, J. F. Kepros, T. Barbera, M. Y. Ho, L. B. Chen, R. A. Lerner and R. H. Bruce, *Proc. Natl. Acad. Sci. U. S. A.*, 2004, **101**, 10501–10504.
8 M. K. Baker, K. Mikhitarian, W. Osta, K. Callahan, R. Hoda, F. Brescia, R. Kneuper-Hall, M. Mitas, D. J. Cole and W. E. Gillanders, *Clinical Cancer Research*, 2003, **9**, 4865–4871.
9 O. Lara, X. Tong, M. Zborowski and J. J. Chalmers, *Exp. Hematol.*, 2004, **32**, 891–904.
10 W. J. Allard, J. Matera, M. C. Miller, M. Repollet, M. C. Connelly, C. Rao, A. G. Tibbe, J. W. Uhr and L. W. Terstappen, *Clin. Cancer Res.*, 2004, **10**, 6897–6904.
11 S. Riethdorf, H. Fritsche, V. Muller, T. Rau, C. Schindlbeck, B. Rack, W. Janni, C. Coith, K. Beck, F. Janicke, S. Jackson, T. Gornet, M. Cristofanilli and K. Pantel, *Clin. Cancer Res.*, 2007, **13**, 920–928.
12 D. W. Bell and D. A. Haber, *Clin. Cancer Res.*, 2006, **12**, 3875–3877.
13 A. M. Sieuwerts, J. Kraan, J. Bolt, P. van der Spoel, F. Elstrodt, M. Schutte, J. W. Martens, J. W. Gratama, S. Sleijfer and J. A. Foekens, *J. Natl. Cancer Inst.*, 2009, **101**, 61–66.
14 M. Hosokawa, T. Hayata, Y. Fukuda, A. Arakaki, T. Yoshino, T. Tanaka and T. Matsunaga, *Anal. Chem.*, 2010, **82**, 6629–6635.
15 S. C. Hur, A. J. Mach and D. Di Carlo, *Biomicrofluidics*, 2011, **5**, 022206.
16 H. S. Moon, K. Kwon, S. I. Kim, H. Han, J. Sohn, S. Lee and H. I. Jung, *Lab Chip*, 2011, **11**, 1118–1125.
17 S. Nagrath, L. V. Sequist, S. Maheswaran, D. W. Bell, D. Irimia, L. Ulkus, M. R. Smith, E. L. Kwak, S. Digumarthy, A. Muzikansky, P. Ryan, U. J. Balis, R. G. Tompkins, D. A. Haber and M. Toner, *Nature*, 2007, **450**, 1235-U1210.
18 S. L. Stott, C. H. Hsu, D. I. Tsukrov, M. Yu, D. T. Miyamoto, B. A. Waltman, S. M. Rothenberg, A. M. Shah, M. E. Smas, G. K. Korir,

F. P. Floyd, A. J. Gilman, J. B. Lord, D. Winokur, S. Springer, D. Irimia, S. Nagrath, L. V. Sequist, R. J. Lee, K. J. Isselbacher, S. Maheswaran, D. A. Haber and M. Toner, *Proc. Natl. Acad. Sci. U. S. A.*, 2010, **107**, 18392–18397.
19 S. T. Wang, K. Liu, J. A. Liu, Z. T. F. Yu, X. W. Xu, L. B. Zhao, T. Lee, E. K. Lee, J. Reiss, Y. K. Lee, L. W. K. Chung, J. T. Huang, M. Rettig, D. Seligson, K. N. Duraiswamy, C. K. F. Shen and H. R. Tseng, *Angew. Chem., Int. Ed.*, 2011, **50**, 3084–3088.
20 S. Y. Zheng, H. K. Lin, B. Lu, A. Williams, R. Datar, R. J. Cote and Y. C. Tai, *Biomed. Microdevices*, 2011, **13**, 203–213.
21 J. Sun, C. C. Stowers, E. M. Boczko and D. Li, *Lab Chip*, 2010, **10**, 2986–2993.
22 J. Sun, Y. Gao, R. J. Isaacs, K. C. Boelte, C. P. Lin, E. M. Boczko and D. Li, *Anal. Chem.*, 2012, **84**, 2017–2024.
23 Y. Kang, D. Li, S. A. Kalams and J. E. Eid, *Biomed. Microdevices*, 2008, **10**, 243–249.
24 P. G. Schiro, M. Zhao, J. S. Kuo, K. M. Koehler, D. E. Sabath and D. T. Chiu, *Angew. Chem., Int. Ed.*, 2012, **51**, 1–6.
25 P. T. Went, A. Lugli, S. Meier, M. Bundi, M. Mirlacher, G. Sauter and S. Dirnhofer, *Hum. Pathol.*, 2004, **35**, 122–128.
26 S. J. Tan, L. Yobas, G. Y. H. Lee, C. N. Ong and C. T. Lim, *Biomed. Microdevices*, 2009, **11**, 883–892.
27 G. Vona, A. Sabile, M. Louha, V. Sitruk, S. Romana, K. Schutze, F. Capron, D. Franco, M. Pazzagli, M. Vekemans, B. Lacour, C. Brechot and P. Paterlini-Brechot, *Am. J. Pathol.*, 2000, **156**, 57–63.
28 S. Y. Zheng, J. Q. Liu and Y. C. Tai, *J. Microelectromech. Syst.*, 2008, **17**, 1029–1038.
29 L. Zabaglo, M. G. Ormerod, M. Parton, A. Ring, I. E. Smith and M. Dowsett, *Cytometry*, 2003, **55A**, 102–108.
30 S. Zheng, H. Lin, J. Q. Liu, M. Balic, R. Datar, R. J. Cote and Y. C. Tai, *J. Chromatogr., A*, 2007, **1162**, 154–161.
31 D. Di Carlo, *Lab Chip*, 2009, **9**, 3038–3046.
32 D. R. Gossett, W. M. Weaver, A. J. Mach, S. C. Hur, H. T. K. Tse, W. Lee, H. Amini and D. Di Carlo, *Anal. Bioanal. Chem.*, 2010, **397**, 3249–3267.
33 D. R. Gossett and D. Di Carlo, *Anal. Chem.*, 2009, **81**, 8459–8465.
34 J. J. Zhu, T. R. J. Tzeng and X. C. Xuan, *Electrophoresis*, 2010, **31**, 1382–1388.
35 D. Di Carlo, D. Irimia, R. G. Tompkins and M. Toner, *Proc. Natl. Acad. Sci. U. S. A.*, 2007, **104**, 18892–18897.
36 S. S. Kuntaegowdanahalli, A. A. S. Bhagat, G. Kumar and I. Papautsky, *Lab Chip*, 2009, **9**, 2973–2980.
37 J. Seo, M. H. Lean and A. Kole, *J. Chromatogr., A*, 2007, **1162**, 126–131.
38 W. C. Lee, A. A. S. Bhagat, S. Huang, K. J. Van Vliet, J. Han and C. T. Lim, *Lab Chip*, 2011, **11**, 1359–1367.
39 A. A. S. Bhagat, H. W. Hou, L. D. Li, J. Y. Han and C. T. Lim, *Lab Chip*, 2011, **11**, 1870–1878.
40 A. J. Mach, J. H. Kim, A. Arshi, S. C. Hur and D. Di Carlo, *Lab Chip*, 2011, **11**, 2827–2834.
41 E. S. Asmolov, *J. Fluid Mech.*, 1999, **381**, 63–87.
42 S. A. Morsi and A. J. Alexander, *J. Fluid Mech.*, 1972, **55**, 193–208.
43 D. Di Carlo, J. F. Edd, K. J. Humphry, H. A. Stone and M. Toner, *Phys. Rev. Lett.*, 2009, **102**, 094503.
44 A. A. S. Bhagat, S. S. Kuntaegowdanahalli and I. Papautsky, *Lab Chip*, 2008, **8**, 1906–1914.
45 Y. Sun, Z. Huang, K. X. Yang, W. W. Liu, Y. Y. Xie, B. Yuan, W. Zhang and X. Y. Jiang, *PLoS One*, 2011, **6**, e28156.
46 Y. Y. Xie, W. Zhang, L. M. Wang, K. Sun, Y. Sun and X. Y. Jiang, *Lab Chip*, 2011, **11**, 2819–2822.
47 J. S. Sun, S. K. Vajandar, D. Y. Xu, Y. J. Kang, G. Q. Hu, D. Q. Li and D. Y. Li, *Microfluid. Nanofluid.*, 2009, **6**, 589–598.
48 D. Di Carlo, J. F. Edd, D. Irimia, R. G. Tompkins and M. Toner, *Anal. Chem.*, 2008, **80**, 2204–2211.
49 S. C. Hur, N. K. Henderson-MacLennan, E. R. B. McCabe and D. Di Carlo, *Lab Chip*, 2011, **11**, 912–920.
50 J. S. Kuo, Y. X. Zhao, P. G. Schiro, L. Y. Ng, D. S. W. Lim, J. P. Shelby and D. T. Chiu, *Lab Chip*, 2010, **10**, 837–842.
51 J. Nam, H. Lim, D. Kim, H. Jung and S. Shin, *Lab Chip*, 2012, **12**, 1347–1354.

